

AperTO - Archivio Istituzionale Open Access dell'Università di Torino

EXAFS wavelet transform analysis of Cu-MOR zeolites for the direct methane to methanol conversion

This is the author's manuscript

Original Citation:

Availability:

This version is available <http://hdl.handle.net/2318/1758295> since 2020-10-13T17:42:16Z

Published version:

DOI:10.1039/d0cp01257b

Terms of use:

Open Access

Anyone can freely access the full text of works made available as "Open Access". Works made available under a Creative Commons license can be used according to the terms and conditions of said license. Use of all other works requires consent of the right holder (author or publisher) if not exempted from copyright protection by the applicable law.

(Article begins on next page)

EXAFS Wavelet Transform analysis of Cu-MOR zeolites for the direct methane to methanol conversion

Andrea Martini,^{a,b} Matteo Signorile,^a Chiara Negri,^{a,c} Karoline Kvande,^c Kirill A. Lomachenko,^d Stian Svelle,^c Pablo Beato,^e Gloria Berlier,^a Elisa Borfecchia,^{*a} Silvia Bordiga^{a,c}

Dedicated to Prof. Carlo Lamberti

^{a.} Department of Chemistry, NIS Center and INSTM Reference Center, University of Turin, via P. Giuria 7, 10125 Turin, Italy. E-mail: elisa.borfecchia@unito.it

^{b.} Smart Materials, Research Institute, Southern Federal University, Sladkova Street 174/28, 344090 Rostov-on-Don, Russia.

^{c.} Center for Materials Science and Nanotechnology (SMN), Department of Chemistry, University of Oslo, 1033 Blindern, 0315 Oslo, Norway.

^{d.} European Synchrotron Radiation Facility, 71 avenue des Martyrs, CS 40220, 38043 Grenoble Cedex 9, France.

^{e.} Haldor Topsøe A/S, Haldor Topsøes Allé 1, DK-2800 Kgs. Lyngby, Denmark.

Abstract

Cu-exchanged zeolites have been shown to possess Cu-oxo species active towards the direct methane to methanol (DMTM) conversion, carried out through a chemical-looping approach. Different Cu-zeolites have been investigated for the DMTM process, with Cu-mordenite (Cu-MOR) being among the most active. In this context, an accurate determination of the local structure and nuclearity of selective Cu-oxo species responsible for an efficient DMTM conversion still represents an ongoing challenge for characterization methods, including synchrotron-based X-ray absorption spectroscopy (XAS). Herein, we explore the potential of an alternative analysis of Extended X-ray Absorption Fine Structure (EXAFS) data using Wavelet Transform (WT) to enhance the technique sensitivity to multimeric Cu species hosted in the MOR framework. Combining *ex situ* XAS measurements under model red-ox conditions with *in situ* data collected after the key steps of the DMTM process, we demonstrate how EXAFS-WT enables unambiguous detection of Cu-Cu scattering contributions from multimeric Cu-species. As also confirmed by complementary *in situ* IR spectroscopy results, these are observed to dynamically respond to the chemical environment over the different conditions probed. We finally report a proof-of-concept EXAFS fit using the WT representation, applied to the structural refinement of O₂-activated Cu-MOR. The fitting results reveal a Cu local coordination environment consistent with mono-(μ -oxo) di-copper cores, with Cu-Cu separation of ~ 3.1 Å, paving the way to future applications and developments of the method in the field of Cu-zeolites research and beyond.¹

Introduction

1. Introduction

Methane is an abundant feedstock that can be extracted inexpensively from shale gas and other sources, such as oil extraction sites. Hundreds of billion cubic meters of methane are flared or vented into the atmosphere every year, due to the high cost for transportation, with tremendous impact on climate

change.¹ The possibility to develop small-scale environment-friendly chemical processes (as compared to the current technology based on steam reforming) for on-site direct conversion of methane to high added value commodities such as methanol would have a remarkable effect on the massive global impact of the chemical industry.² The search for a direct route to convert methane to methanol (DMTM) is considered an 'Holy Grail' in chemistry and in catalysis.³ Many aspects make this reaction unfavourable, such as the high stability of the C-H bond in the reactant, the high reactivity of the product (favouring over-oxidation), the 'spin-dilemma' and unbalanced mass/electron stoichiometry when using O₂ as oxidant.⁴

To overcome these limitations, an approach based on the use of Cu-exchanged zeolites has been proposed.⁵ In this context, Cu-zeolites (ZSM-5, Mordenite, Chabazite, Omega, and others) are involved in a 'chemical-loop' process, where active and selective 'Cu-oxo' species are formed by high temperature O₂ activation, followed by methane exposure and extraction of the product with water vapour.⁶⁻⁸ The productivity of the process is still very low, making it appear mainly an academic playground. However, important advances towards industrial applications were reported, concerning the use of water for an anaerobic process⁹ and the possibility to carry out the chemical loop steps (O₂ activation, CH₄ dosage, CH₃OH extraction), in isothermal conditions.^{10, 11}

The structure and nuclearity of the selective Cu-oxo species responsible for an efficient DMTM process is still lively debated in the literature. Focusing on Cu-MOR, many groups point to the role of di-copper species, such as the mono(μ -oxo)dicopper core.^{9, 12-16} Nonetheless, trinuclear⁷ or even larger¹⁷ Cu oxo clusters have been proposed as active sites for DMTM conversion over this zeolite. Parallel studies have explored the impact of Si/Al ratio on Cu-speciation in activated Cu-MOR, highlighting how both monomeric and multimeric Cu-species can be present and active towards DMTM.¹⁸ As it is now well established for Cu-CHA, extensively studied also in connection with deNO_x applications,¹⁹⁻²² it is clear that Cu-speciation in the MOR zeolite is dynamically driven by compositional, synthesis and pre-treatment parameters, representing an ongoing challenge for characterization. Overall, analytic methods capable to pinpoint nuclearity and local structure of Cu-species formed under process-relevant conditions are of utmost importance to progress the field of DMTM over Cu-zeolites.

In this context, X-ray absorption spectroscopy (XAS) at synchrotron sources has been widely employed to characterize Cu-zeolites in their activated state,^{5, 13, 16, 23, 24} as well as during the DMTM reaction.^{6-9, 25-28} Indeed, XAS offers element-selective information about the local structural and electronic properties of the Cu-ions hosted, without long-range order, in the zeolite framework.^{21, 29, 30} Moreover, due to the high penetration depth of hard X-rays in matter, *in situ* and *operando* experiments carried out under controlled conditions (temperature, gas feed) can be performed in a relatively easy way.²⁹

Analysis of Cu K-edge XAS spectra in the X-ray Absorption Near Edge Structure (XANES) region, remarkably rich in spectroscopic fingerprints,^{31, 32} has enabled the determination of oxidation state and coordination

geometry of dehydrated Cu-species in the MOR framework.^{8, 13, 24-26} Here, the use of multivariate curve resolution (MCR) techniques,^{28, 33, 34} eventually coupled with high-energy resolution fluorescence-detected XANES^{16, 35} has been particularly useful to resolve the spectral signatures of different Cu-species within the absorber-element averaged XAS signal. Nonetheless, based on previous DFT-assisted XANES simulations for mono- and di-copper species hosted in the MOR zeolite,³⁶ it is evident that XANES lacks of specific sensitivity to the nuclearity of the Cu-sites, especially when species with the same first-shell coordination motifs are compared.

With this respect, conclusive information should be, in principle, accessible from Extended X-ray Absorption Fine Structure (EXAFS) analysis, due to the direct sensitivity of this spectral region to the local coordination environment of the Cu ions. However, also in this case, specific difficulties subsist, challenging the standard EXAFS analysis based on Fourier Transform (FT) and *R*-space data interpretation/fitting. The first peak observed in the FT-EXAFS of activated Cu-MOR, and in general of Cu-zeolites, is well established to arise from single-scattering (SS) contributions involving framework (O_{fw}) and extra-framework (O_{efw}) oxygen atoms.^{6, 13, 23, 37}

However, the interpretation of the EXAFS signal at higher distances is more controversial. Indeed, in this *R*-space range, multiple elemental contributions and scattering interactions are expected to coexist, including: (i) SS contributions from second-shell framework Al/Si atoms (present in both mono- and multi-copper species); (ii) Cu-Cu SS paths characteristic of multi-copper species; (iii) possibly, multiple-scattering (MS) contributions involving first-shell atoms. Such contributions are difficult, if not impossible, to disentangle in the conventional *R*-space signal representation, so that the actual existence and nature of low-nuclearity multimetric copper species remains often elusive.

Driven by these motivations, we are currently exploring an alternative approach, based on Wavelet Transform (WT) analysis,³⁸⁻⁴⁰ for the visualization and analysis of the EXAFS spectra of Cu-zeolites.^{36, 41, 42} This strategy combines information coming from both *k*-space and *R*-space. Here, the element-dependent *k*-space localization of EXAFS backscattering amplitude factors $F(k)$ is exploited to effectively discriminate among scattering contributions involving different atomic neighbours (primarily framework Al/Si and Cu), while maintaining structural sensitivity to interatomic distances.

Herein, we apply WT-EXAFS analysis to XAS data collected on Cu-MOR, one of the most promising zeolites towards DMTM,¹⁶ aiming at enhancing the sensitivity of EXAFS to multimetric Cu species. We initially focus on *ex situ* measurements, collected for Cu-MOR samples with different compositional characteristic (Si/Al, Cu/Al), investigated under model conditions yielding Cu(I) or Cu(II) species. Then, capitalizing on the obtained insights, we apply EXAFS WT to *in situ* XAS data collected after the key steps of the DMTM process over the most active Cu-MOR material.¹⁶ In this case XAS analysis is paralleled by *in situ* IR spectroscopy, securing a complementary view on the framework vibrational properties, as well as on their dynamical

response to Cu-species hosted inside the zeolite lattice. Finally, having shown the potential of qualitative EXAFS-WT analysis to visually identify Cu-Cu scattering contributions, we make a step further proposing a novel EXAFS fitting procedure using the WT representation.

2. Experimental

2.1 *Ex situ* and *in situ* X-ray absorption spectroscopy (XAS)

In this work, we present the results obtained from analysis of two XAS datasets, both collected at the BM23 beamline⁴³ of the ESRF. The first one regards an *ex situ* experiment based on the measurement of the Cu K-edge XAS of four Cu-exchanged mordenite zeolites (Cu-MOR), denoted here with the following notation: $x\text{Cu-HMOR}(y)$, where $x=\text{Cu/Al}$ and $y=\text{Si/Al}$ ratios. On this basis, the four samples will be indicated as 0.24Cu-HMOR(7), 0.18Cu-HMOR(7), 0.36Cu-HMOR(11) and 0.1Cu-HMOR(11). The synthesis of the samples is described in ref.²⁵ Each material was prepared in the form of a self-supporting pellet of optimized mass and activated inside a devoted glass cell equipped with Kapton windows, which allows to perform measurements under controlled atmosphere. Each sample underwent to two distinct treatments: (i) *vacuum activation* – heating in vacuum from room temperature (RT) to 400 °C, keeping the sample at 400 °C for 1 h and cooling down to RT, always in vacuum; (ii) *vacuum activation + O₂ 200 °C* - starting from the vacuum-activated sample, pre-heating in vacuum up to 80 °C, sending 100 mbar of O₂ and heat from 80 °C to 200 °C, keeping the sample at 200 °C for 1 h in O₂, cooling down to RT (always in O₂), finally outgassing O₂ from the cell at RT. In both cases, the Cu-MOR samples were measured at RT. The related XAS spectra were collected in transmission mode using a Si(111) double-crystal monochromator while the incident (I_0) and transmitted (I_1) X-ray intensities were detected in the range within 8880 and 9995 eV (25 min/scan) using ionization chambers filled with a mixture of He and Ar. The third ionization chamber (I_2) was finally used for the simultaneous collection of the XANES spectrum of a Cu metal foil for the energy calibration procedure.

The second dataset refers to an *in situ* experiment where Cu K-edge XAS data were acquired in order to monitor each step of the DMTM process over the 0.18Cu-HMOR(7) zeolite, yielding the best methanol productivity throughout the whole compositional series (0.47 mol CH₃OH/mol Cu, based on laboratory fixed-bed tests conducted adopting the same reaction protocol used during *in situ* XAS experiments).^{16, 26} Herein, the pelletized sample (always with optimized mass for transmission mode XAS) was hosted in an *ad hoc* reactor cell developed at the BM23/ID24 beamlines of the ESRF.⁴⁴ After fixing the sample pellet inside, the reactor cell was closed and connected to a dedicated gas flow setup for the DMTM reaction. A heating/cooling rate of 5 °C/min and a total flow rate of 8 ml/min was employed for all the steps, including O₂-activation at 500 °C (480 min, 100% O₂), CH₄-loading at 200 °C (360 min, 100% CH₄), and steam-assisted CH₃OH extraction at 200 °C (ca. 60 min). The extraction process was performed by flowing Ar/He through

a saturator with deionized water at 44 °C. A detailed description of the followed protocol can be found in ref.²⁶ As for the *ex situ* experiment, the *in situ* measurements were collected in transmission mode using the same monochromator in an energy range within 8880 and 9726 eV (ca. 20 min/scan).

For both the experiments, the collected XAS spectra were aligned in energy and normalized to unity edge jump using the Athena software from the Demeter package.⁴⁵ The $\chi(k)$ EXAFS signals were also extracted using the same program. For the scans relative to the *ex situ* experiment, the Fourier transforms (FT) of the EXAFS spectra were obtained by transforming the $k^2\chi(k)$ functions in the (2.4–13.0) Å⁻¹ range. For the *in situ* experiment, a shorter range (2.4-10.5) Å⁻¹ was chosen due to the lower S/N ratio at high k -values, principally induced by the higher data collection temperature.

2.2 Wavelet Transform (WT) analysis

It is possible to assert that if two or more groups of different atoms are localized at close distances around the absorber, their contributions in the direct space R overlap, becoming often indistinguishable.³⁸⁻⁴⁰ This makes the classical Fourier transform (FT) analysis of the EXAFS spectrum rather uninformative. However, from a detailed analysis of the EXAFS equation, it is possible to observe that the path contributions arising from the different scatterers surrounding the absorbing atom are localized in the k -space, principally thanks to their backscattering amplitude factors $F(k)$. This term depends strongly on the scatterer atomic number Z . In particular it is possible to observe that signals produced by heavier atoms, being characterized by larger values of $F(k)$, are usually localized at higher wavenumbers than lighter atoms,^{36, 40-42} see Figure 2b. This evidence can be exploited to enhance the sensitivity of EXAFS analysis by a modern spectral processing technique, called Wavelet Transform (WT) analysis,^{38, 39} which can efficiently replace the *classical* FT representation of the EXAFS spectrum. WT is able to provide a 2D representation of the EXAFS spectrum, revealing, in this way, the signal features in k and R -spaces simultaneously.

The WT of a general k^n -weighted EXAFS spectrum is defined as:

$$W_{\chi}^{\psi}(a, b) = \frac{1}{\sqrt{a}} \int_{-\infty}^{+\infty} dk' k'^n \chi(k') \psi^* \left(\frac{k' - b}{a} \right) \quad (1)$$

This equation can be seen as the inner product between the k^n -weighted EXAFS spectrum $\chi(k)$ and a defined window function ψ , called *mother wavelet* or simply wavelet (where the apex ψ^* denotes the complex conjugate of ψ), which must decay at zero for higher values of $|k'|$. Herein, the signal $\chi(k)$ is analysed through a set of train-waves (wavelets) that are shifted by b units in the k -space and distorted by a factor a in order to take account of the local frequencies of the signal.^{34, 41, 46} The variables a and b are connected to k - and R -space by the following relations: $a = \eta/2R$ and $b = k$.

In this work, the Morlet wavelet, expressed in the following form, was used:

$$\psi(k) = \frac{1}{\sqrt{2\pi}\sigma} \exp(i\eta k) \exp(-k^2/2\sigma^2) \quad (2)$$

Where i denotes the complex unit while η and σ are two parameters regulating the wavelet resolution in R and k spaces.^{38, 47} More precisely, η represents the frequency of a sine wave convoluted by a gaussian with standard deviation σ , that acts localizing the oscillation in the k space. The selection of appropriate values for these two parameters is critical and must be optimized on a case-by-case basis in order to have the best visualization of the desired spectral features. In fact, it is worth mentioning that the WT distributes the signal information over some k - R cells, usually named as *uncertainty* or *Heisenberg boxes*,⁴⁷ which, for the Morlet wavelet, can be expressed in the following form:

$$\left[k \pm \frac{\eta\sigma}{\sqrt{2}R} \right] \times \left[R \pm \frac{R}{\sqrt{2}\eta\sigma} \right] \quad (3)$$

On the basis of eq. (3), it is possible to see that the resolution in k and R space are inversely proportional; this means that a good resolution in the k -space always implies a loss of information in the related R -space, and vice-versa.

2.2.1 Fitting an EXAFS spectrum using the WT representation

The WT EXAFS fitting procedure is implemented following the scheme exploited by IFEFFIT.⁴⁸ Starting from an initial guess structure, a FEFF input file is created selecting a determined atom as the absorber. Afterwards, the FEFF6.0L^{49, 50} software is used to generate the *feffnnn.dat* file for each path. Finally, for each data files, the k -dependent arrays obtained by FEFF,⁵¹ are linearly interpolated on the k -grid of the experimental EXAFS spectrum and then used to build up the single path contribution $\chi_i(k)$, which is given by the following expression:

$$\begin{aligned} \chi_i(k) = & \frac{S_{0i}^2 N_i F_i(k)}{k(\Delta R_i + R_i)^2} \exp\{i[2kR_i + \delta_i(k)]\} \\ & \times \exp[i(2p\Delta R_i - 4p\sigma_i^2/R_i)] \times \exp\left[-\frac{2R_i}{\lambda(k)} - 2p^2\sigma_i^2\right] \end{aligned} \quad (4)$$

Here, k is defined as: $k = \sqrt{k_0^2 - 2m_e\Delta E_0/\hbar^2}$, ΔE_0 is an energy edge shift, m_e is the electron mass while k_0 is the unshifted k -array.

In eq. (4) the following factors appear: S_{0i}^2 is the amplitude reduction factor, N_i is the number of scattering atoms of type i , $F_i(k)$ is the backscattering amplitude factor, $\delta_i(k)$ is the total phase shift term while $\lambda(k)$ represents the electron mean-free path. Finally, the Debye-Waller factor σ_i^2 and the path length variation ΔR_i correspond to the first two cumulants of the atomic pair distribution for the selected path, while p is the complex-valued wavelength, introduced to account for the thermal or configurational disorder.⁵¹ The

fitting parameters are, in this way: S_{0i}^2 , N_i , σ_i^2 , ΔE_0 and ΔR_i . Once that for each selected path the relative EXAFS signal has been calculated using eq. (4), the theoretical total signal is generated summing all the contributions together:

$$\begin{aligned}\chi^{THEORY}(k) \\ = \sum_i \chi_i(k)\end{aligned}\quad (5)$$

The theoretical signal $\chi^{THEORY}(k)$ can be involved in the calculation of the residual complex function for the wavelet filtered data, as:

$$f(k, R) = \Re \left[W_{\chi^{DATA}}^{\psi}(k, R) - W_{\chi^{THEORY}}^{\psi}(k, R) \right] + \Im \left[W_{\chi^{DATA}}^{\psi}(k, R) - W_{\chi^{THEORY}}^{\psi}(k, R) \right] \quad (6)$$

The output of eq. (6), calculated in the Δk and ΔR ranges of interest, is a two dimensional grid which can be arranged to a one dimensional array, indicated here as f_i , including the real and imaginary parts, having in this way a length w equal to two times the length of the product of the k and R lists. On this basis, it is possible to define a metric function Ξ^2 defined as:⁵²

$$\Xi^2(k, R) = \frac{1}{w} \sum_{i=1}^w [f_i(k, R)]^2 \quad (7)$$

The function Ξ^2 can be properly minimized using different algorithms: in our case we adopted the classical Levenberg-Marquard method⁵³ used also in IFEFFIT.⁵¹ Finally, the errors and the correlation values associated to the best-fit derived parameters, are obtained by the inverse of the Hessian (H^{-1}), calculated for Ξ^2 , in correspondence of its minimum value. It is possible to demonstrate that, in fact, the diagonal elements of H^{-1} are the squared parameter errors while the off-diagonal elements, when divided by the square root of the product of the corresponding diagonal elements provide the related correlation values.^{52, 54, 55} The WT fit routine described in this article has been realised in Python using the Scipy and LMFIT packages.^{56, 57}

2.3 *In situ* infrared (IR) spectroscopy

The *in situ* infrared (IR) spectroscopy measurements were performed in transmission mode on 0.18Cu-HMOR(7), in a sample environment closely similar to the one adopted in the *in situ* XAS measurements. In detail, the catalyst was prepared as a thin self-supporting pellet and mounted in the heating element of an AABSPEC (5 #2000-A multimode) cell equipped with KBr windows. The activation/reaction protocol follows the one proposed for XAS, but the time dedicated to isothermal steps was reduced. More specifically, the sample was activated under 10 ml/min of pure O₂, ramping from RT to 500 °C with a rate of 5 °C/min and keeping this temperature for 120 min. After reducing the temperature to 200 °C, the O₂ was purged by a

He flow (10 ml/min) for 15 min and then the oxidized sample was contacted with pure CH₄ (10 ml/min) for 60 min at the same temperature. Finally, the steam-assisted CH₃OH extraction was performed again at 200 °C, for 60 min under 10 ml/min of H₂O saturated He (saturator temperature: 25 °C). The same protocol (but limited to the oxidative step only) was adopted in the activation of the parent HMOR(7) zeolite, that we report for comparison. The IR measurements were performed on a Bruker Invenio R Fourier Transform spectrophotometer, equipped with a cryogenic MCT detector, at a resolution of 2 cm⁻¹ by averaging 32 scans per spectrum.

3. Results and Discussion

3.1 EXAFS WT for reduced and oxidized Cu-MOR: impact of treatment and composition

Figure 1a,b reports an overview of the *ex situ* XAS data, collected at RT for the investigated Cu-MOR zeolites, after thermal treatment in vacuum and in O₂, according to the protocol described in Section 2.1. Notably, as previously reported for Cu-CHA zeolites,²³ in the as-prepared materials, Cu ions mostly occur as mobile Cu(II) aquo complexes, with XAS features equivalent to those observed for a reference Cu(II)/H₂O solution. Considering the XANES spectra obtained for the vacuum-activated samples, it is clear that, for all the Cu-MOR compositions, the Cu ions in the systems exist in a virtually pure Cu(I) oxidation state. Cu(I) species are formed *via* self-reduction, well known to occur in Cu-zeolites upon thermal treatment under vacuum or inert gas flow.^{13, 23, 58, 59} Within the resolution of these measurements, no trace of the pre-edge peak, arising from 1s → 3d transition in d⁹ Cu(II) ions, is in fact detected. All these XANES spectra are dominated by a prominent rising-edge peak at 8982.5 eV, assigned to the 1s → 4p transition in Cu(I) ions. Overall, all the acquired XANES spectra for the Cu(I) state closely resemble the one of the linear [Cu(I)(NH₃)₂]⁺ model compound.^{24, 60} Previous studies have explored by DFT the coordination of Cu(I) species inside the side-pocket of the MOR zeolite, identified as the most favorable docking site for the Cu ions,⁶¹ considering both isolated and 'coupled' Cu(I) species.²⁴ In both cases, computational modelling confirms a quasi-linear geometry for Cu(I) sites, thus justifying a Cu K-edge XANES spectrum very similar to the one of the perfectly linear [Cu(I)(NH₃)₂]⁺ model compound. Cu(I) ions are coordinated to two O_{fw} with bond angles around 144° and interatomic distances in the 1.98-2.21 Å range. The high-R coordination environment includes a farther O_{fw} atom at ca. 2.3 Å and, at around 2.9 Å, the charge-balancing Al atom and a Si atom of the MOR framework. For the coupled Cu(I)···Cu(I) model, DFT indicates a Cu–Cu distance of ca. 3.6 Å.

Such proposal for local coordination environment of Cu(I) species in MOR consistently reflects in the phase-uncorrected FT-EXAFS. Here, we note a first maximum at 1.5 Å, with a broad shoulder at 2.1 Å. At longer *R*-values, only a broad feature peaking at 2.9 Å is observed. The first shell intensity is comparable with the one observed for the [Cu(I)(NH₃)₂]⁺ model compound, supporting, on average, the presence of two O_{fw} in

the first coordination shell of Cu(I) species. For 0.36Cu-HMOR(11), the EXAFS signal at higher R-values has been previously found consistent with partially overlapped scattering contributions involving framework Al/Si as well as Cu atomic neighbours.²⁴ Nonetheless, the fit results were affected by rather high correlations among the parameters employed to model the Al and Cu scattering paths, translating into a general accuracy loss in the structural refinement. Focusing on the *in situ* XAS of Cu-MOR after exposure to O₂, the related XANES features can be qualitatively interpreted based on previous studies on this topic.^{8, 13, 16, 26} For all the samples, thermal treatment in O₂ up to 200 °C results into oxidation to Cu(II) of most of the Cu-species, characterized as Cu(I) after vacuum activation. Nonetheless, a minor Cu(I) contribution is still detectable, as indicated by the residual peak at 8982.5 eV.

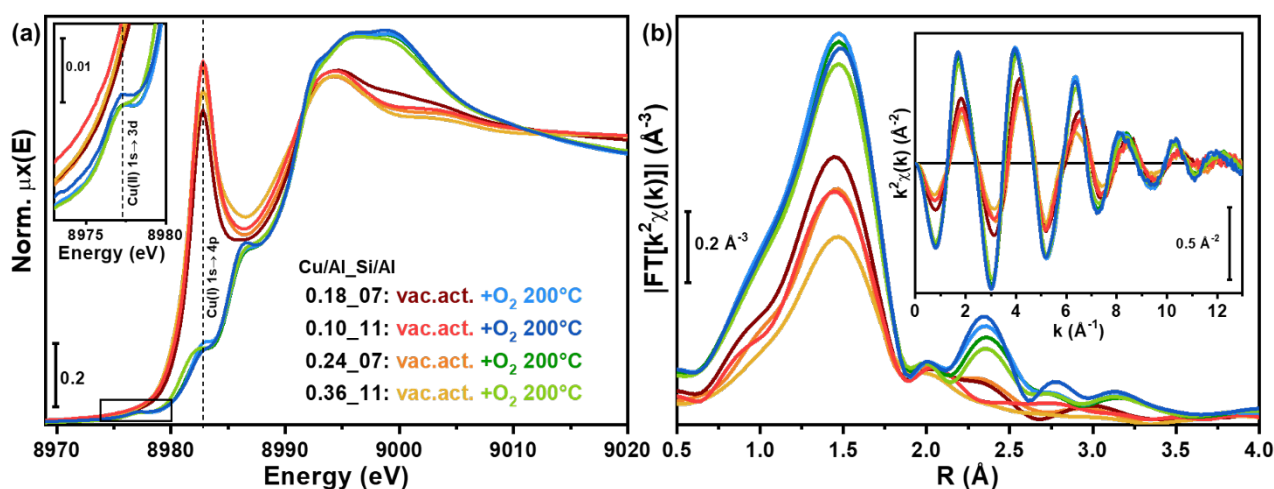


Figure 1. (a) *Ex situ* Cu K-edge XANES spectra for Cu-MOR zeolites with different compositions, obtained after vacuum-activation at 400 °C (warm colours) and exposure to O₂ until 200 °C (cold colours). The inset reports a magnification of the pre-edge peak arising from 1s → 3d transition in d⁹ Cu(II) ions. (b) Correspondent phase-uncorrected moduli of the Fourier transform obtained transforming the k² χ(k) EXAFS signals (showed in the inset), in the 2.4-13.0 Å⁻¹ range, using a Hanning window function with dk=1.

Compared to the spectra collected after vacuum activation, we note that the XANES of the four Cu-MOR zeolites after exposure to O₂ show remarkable similarities. This evidence points to comparable coordination environments for the Cu(II) ions in the zeolite cages across the investigated compositional series.

More pronounced variations are instead visible analysing the EXAFS FT spectra reported in Figure 1b. Here, the first-shell peaks, arising from scattering contributions by framework (O_{fw}) and extra-framework (O_{efw}) oxygen atoms, exhibit almost equivalent intensity. For all the four compositions, a well-defined feature is visible in the second-shell region, peaking at ca. 2.4 Å and extending with rather broad tails until 3.5 Å in the phase-uncorrected EXAFS spectra. Such feature exhibits composition-dependent intensity variations, being more intense for 0.10Cu-HMOR(11) and 0.18Cu-HMOR(7). Based on previous findings,^{13, 16, 36, 41, 42, 61} we expect both scattering paths involving Al/Si atoms from the zeolite framework (for both mono- and

multimeric Cu-species) and Cu–Cu scattering contributions stemming from Cu_xO_y multimeric moieties to contribute in this R -space range.

Due to its sensitivity to the chemical nature of the scatterers surrounding the absorbing atom,⁴⁰ WT can be exploited to validate the existence of Cu–Cu EXAFS paths, providing a more robust assignment to the high- R EXAFS features discussed before, based on classical FT analysis. To this aim, we applied WT analysis to the Cu-MOR EXAFS spectra reported in Figure 1b: an overview of the obtained results is presented in Figure 2.

We chose, for all the wavelet representations, the following set of parameters controlling the WT resolution: $\sigma = 1$ and $\eta = 7$. The reason of this choice must be identified in the fact that, as suggested theoretically,^{15, 36, 61, 62} the typical distances for Cu pairs forming during the investigated treatments fall in the 3-4 Å range, with average values of ~ 3.5 Å. On this basis, we tried to satisfy, for all the representations, the condition of *optimal resolution* at a given distance of interest, as described by Funke et al.⁶³ Here, the authors show that the best discrimination condition for a WT feature, associated to a determined path, is reached for $\sigma = 1$ and $\eta = 2R_{opt}$, where R_{opt} is the real backscattering path distance.

All the WT representations we obtained for Cu-MOR zeolites show a main lobe at low R values (Δk (0-12.5) Å⁻¹ × ΔR (0.5-2.0) Å): Figure 2a reports a representative example for vacuum-activated 0.18Cu-HMOR(7). As described before, this feature is associated with the single scattering contributions (SS) arising from O_{fw} and O_{efw} atoms. The evident elongation of the first lobe toward large k -values should not be connected with the presence of heavier scatterers. Rather, it is explained introducing the concept of spectral broadening. In fact, as showed by Timoshenko et al.⁴⁰ if, for low R -values, the relation $1/a \ll \eta$ is satisfied (see Section 2.2 for the definitions of a and η), the wavelet lobes are distorted in k -space. This is the case of the main lobe for all the WT maps analyzed in this work, where the low- R range allow to satisfy the condition mentioned above.

Figure 2b shows, for the same exemplificative case, a magnification of the WT-EXAFS in the high- R region (2.0-4.0 Å ΔR range). Here, two distinct ‘sub-lobes’ can be visualized: the first one extends at lower k -values, Δk (3-5) Å⁻¹, while the second occurs in the range Δk (5-9) Å⁻¹. Comparing the k -space ranges where these sub-lobes extends with the relevant backscattering amplitude factor curves $F(k)$, also reported in Figure 2b, it is possible to safely assert that the first sub-lobe is dominated by the contributions of lighter elements (O, Al/Si). Conversely, the second sub-lobe peaks at ca. 7 Å⁻¹, precisely matching the k -value where the Cu backscattering function has its maximum. Thus, it can be unambiguously assigned to Cu–Cu scattering contributions.

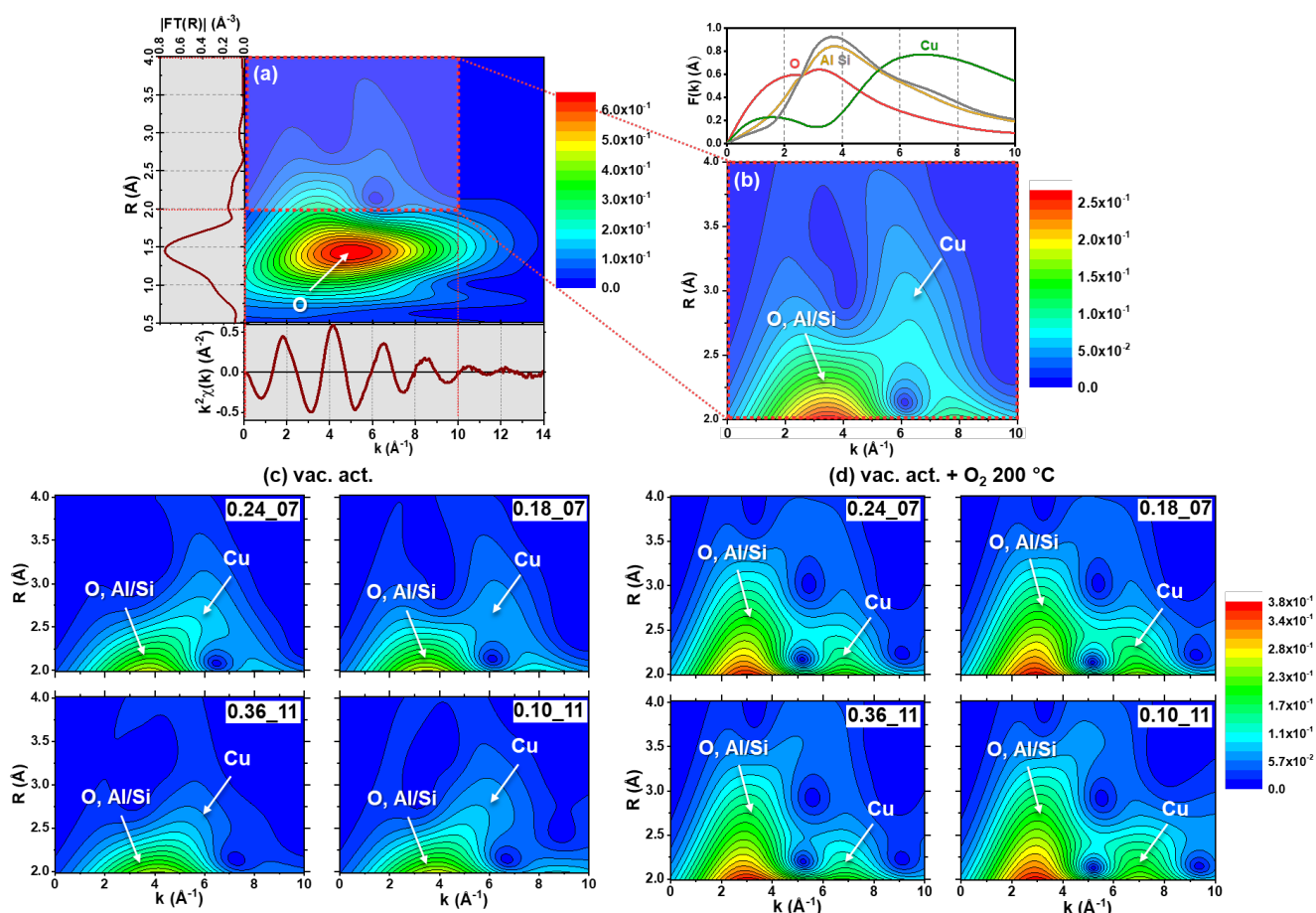


Figure 2. (a) Full-range WT representation of the EXAFS signal for a representative Cu-MOR sample, namely 0.18Cu-HMOR(7), measured at RT after vacuum activation at 400 °C. (b) Magnification of the high- R WT region highlighted by the red dashed box in (a), in the ranges Δk (0-10) \AA^{-1} and ΔR (2-4) \AA . On the top is reported a plot of the relevant backscattering amplitude functions $F(k)$, calculated from FEFF6.0 considering SS paths involving O, Si, Al and Cu scatterers. (c, d) High- R WT region for the *ex situ* EXAFS of Cu-MOR samples (c) after vacuum activation and (d) after subsequent thermal treatment in O_2 up to 200 °C. Compositional characteristics of each sample are indicated by 'Cu/Al_Si/Al' labels. WT sub-lobes stemming from O, Al/Si and Cu atomic neighbours are indicated by white arrows and labels.

Figure 2c compares the high- R WT maps obtained for the vacuum-activated Cu-MOR samples. Here, the two sub-lobes discussed above are always distinguishable, albeit certain differences as a function of the sample composition can be appreciated. These results provide direct structural evidence for the presence of coupled Cu(I)⋯Cu(I) sites,^{24, 64} giving rise to the high- k sub-lobe in the WT maps. However, such feature appears to be more emphasized at lower Si/Al and Cu/Al ratios.

Considering the *ex situ* EXAFS data obtained upon thermal treatment in O_2 , the considerations about the WT main lobe at low R -values for the vacuum-activated materials remain valid. This feature is always associated to the contributions involving O_{fw} and O_{efw} atoms, which may be located at different distances from the Cu centre, but possess the same elemental identity.

Focusing on the high- R WT features summarized in Figure 2d, we also clearly observe for all the investigated compositions the presence of two sub-lobes. Again, their localization in k -space is consistent with major

contributions from framework elements (O, Al/Si) and Cu, for the first and second sub-lobe, respectively. Thus, WT analysis visually demonstrates the presence of framework-coordinated multimetric Cu_xO_y cores, plausibly formed upon interaction of O_2 with the coupled $\text{Cu(I)}\cdots\text{Cu(I)}$ ions detected after vacuum activation.

Comparing these WT representations with the ones obtained after vacuum activation, it becomes evident that the high- R WT features are morphologically different. In particular the high- k sub-lobe, fingerprinting Cu-Cu scattering, is shifted towards lower values of R . At the same time, all the low- k sub-lobes become more intense and expand to higher distances. This behaviour can be rationalized assuming that, upon interaction with O_2 , $\text{Cu}\cdots\text{Cu}$ pairs undergo substantial structural rearrangement, involving contraction of the interatomic distances between the Cu(II) centres in multimetric cores and approaching to the framework of Cu(II) ions.

Similar modifications in the Cu local coordination environment have been previously predicted for Cu-ZSM-5 based on computational modelling.⁶⁴ WT results reported here for Cu-MOR provide direct structural support to these theoretical insights, which would have been difficult to access solely by conventional FT-EXAFS analysis.

In order to better compare the different compositions and treatments explored in this work in term of presence/relative abundance of Cu-Cu contributions, we computed the power density function $\Phi^R(k)$ for all the WT representations.⁶³ This quantity was derived integrating the square of the modulus of the WT over the R -space range $\Delta R=2-4 \text{ \AA}$, containing the Cu-Cu signal contributions. The expression of Φ^R , as a function of k , is given by the following expression:

$$\Phi^R(k) = \int_{R_{min}}^{R_{max}} dR' |W_{\chi}^{\psi}(k, R')|^2 \quad (8)$$

where $R_{min} = 2 \text{ \AA}$, $R_{max} = 4 \text{ \AA}$ while $W^{\psi}(k, R)$ is the wavelet transform representation of the EXAFS signal depending on the choice of used mother function ψ . The results of the integrals calculation for the two treatments are reported in Figure 3.

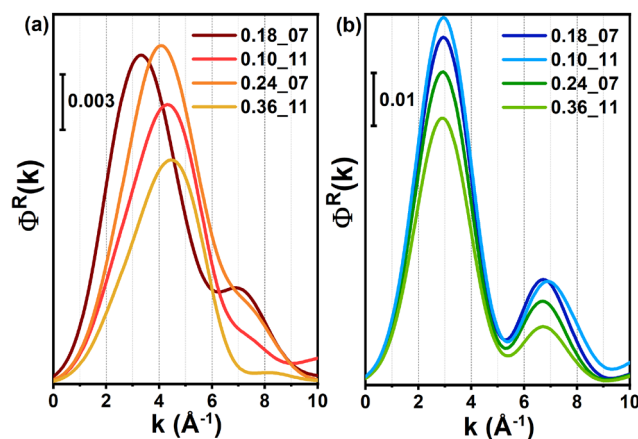


Figure 3. Wavelet power density functions $\Phi^R(k)$ calculated for all the investigated samples from *ex situ* EXAFS data collected (a) after vacuum activation and (b) after subsequent thermal treatment in O₂ up to 200 °C.

All the $\Phi^R(k)$ functions in Figure 3 show a main peak localized at lower k -values followed by a weaker peak localized at around 7 Å⁻¹. The peak FWHM essentially depends on the broadening of the FT-EXAFS features in the relevant R -space range, which is higher after the vacuum activation with respect to the following treatment in O₂. Based on the previous considerations about k -dependency of $F(k)$ functions, the main peak can be associated with SS and MS contributions involving lighter elements (i.e. Al/Si and O_{fw} atoms belonging to the zeolite lattice, as well as O₂-derived O_{efw} after O₂ thermal treatment).

More interesting is the localization of the second peak. This feature corresponds with the maximum of the backscattering amplitude function associated to Cu-Cu SS paths and can be considered as a direct fingerprint for the presence of this kind of contributions, reflecting the high- k sub-lobe in the WT maps discussed before. While the 2D representations in Figure 2c,d bring out simultaneous information in both R - and k -space, the $\Phi^R(k)$ integral functions offer a more practical way to compare different samples/conditions over the relevant R -space range. Indeed, analysing Figure 3a,b, we observe a characteristic trend for the intensity associated with the Cu-Cu feature. At fixed Si/Al ratio in the zeolite framework, the peak intensity is higher for the samples having a lower content of Cu (i.e. Cu/Al = 0.18 and 0.10 at Si/Al = 7 and 11, respectively). The same trend can be observed after both vacuum activation and subsequent thermal treatment in O₂.

This observation points to a ‘saturation’ mechanism driving the formation of Cu-Cu pairs in MOR, whose abundance appears, counterintuitively, to be inversely correlated with the amount of Cu in the sample. Notably, a similar behaviour is well documented for 2Al sites in the same six-member ring of the CHA topology, albeit resulting for Cu-CHA in redox-resistant monomeric Cu(II) ions.^{34,37} Framework composition and synthesis parameters are known to shape the Al distribution in the zeolite lattice,^{65,66} giving rise to a limited number of 2Al docking sites, with Al...Al separation potentially suitable to support multimeric copper moieties once Cu is exchanged into the zeolite. The compositional trend emerging from our analysis suggests that, along dehydration, Cu should preferentially occupy such 2Al sites, resulting into Cu-Cu pair

detectable by EXAFS WT. Once the available *2A*/ exchange sites are saturated, Cu ions will start to populate isolated *1A*/ sites, forming monomeric Cu-species which are silent in the high-*k* region of the WT plane. In this scenario, for the same parent zeolite, higher Cu-loading translates in a higher relative abundance of mono-copper species over total Cu in the system. Remembering that XAS is an absorber-averaged technique, this causes an abatement of the spectral features associated to multimeric configurations (sublobes and peaks around 7 \AA^{-1} in Figure 2c,d and Figure 3a,b, respectively) in the EXAFS-WT response, representing an average over all the Cu-species present weighted by their relative abundance.

3.2 Following by the DMTM reaction over 0.18Cu-HMOR(7)

In this section, we move from *ex situ* studies under model red-ox conditions to *in situ* results obtained by IR and XAS spectroscopies at the key steps of the DMTM process over 0.18Cu-HMOR(7). The two techniques enable to monitor, in a synergic way, the vibrational and acidic properties of the zeolite as well as the dynamic evolution of Cu local environment along the reaction. The latter is probed either directly through EXAFS-WT analysis or indirectly, by monitoring framework modes perturbed by the presence of close cations in the IR spectra. We selected this specific sample due to its outstanding activity towards the target reaction, resulting in a methanol productivity per Cu of 0.47 mol/mol, at optimal process conditions.^{16, 26} By combining MCR analysis of HERFD XANES data with DMTM testing at consistent conditions, we have also shown how for this specific Cu-MOR sample, CH₄ is activated over a dicopper(II) site, involving the large majority of the Cu ions in the system.¹⁶

3.2.1 Complementary insights on O₂-activation by *in situ* IR

Figure 4 illustrates the IR spectra evolution for 0.18Cu-HMOR(7) during activation in oxygen flow at 500 °C. At increasing dehydration, as achieved during the temperature ramp, a sharp and weak band progressively defines at 3745 cm^{-1} . This peak is ascribed to the presence of isolated silanols, most probably terminating at the external surfaces of the MOR primary particles. The low intensity of this feature correlates with the large particle size (hundreds of nm to some μm) of the 0.18Cu-HMOR(7) particles (see Supporting Information of ref.¹⁶ for electron microscopy characterization). The same signal is observed with identical intensity in the spectrum of the activated HMOR(7). In the parent zeolite a complex band with a maximum at 3590 cm^{-1} , tailed toward lower frequencies and an evident shoulder at 3640 cm^{-1} are observed, testifying of a large heterogeneity of Brønsted acidic sites.^{67, 68} In the transparency windows, instead, no bands are observed. In the case of 0.18Cu-HMOR(7), in the $\nu(\text{OH})$ region, along the activation (from the bold black to the bold red curves) we observe the removal of adsorbed water, testified by the progressive erosion of the intense a broad band extending from 3650 to 2500 cm^{-1} .

The main features of the 0.18Cu-HMOR(7) spectrum obtained at the end of O₂ activation, compared to those of the parent material, are the following: (i) an identical profile of the silanol peak; (ii) the substantial erosion of the main band associated to the strong Brønsted acidic sites (components at 3605 and at 3590 cm⁻¹); (iii) a modest change in the intensity of the component at 3640 cm⁻¹, possibly ascribed to ν(OH) groups of Al-OH species in defects. Furthermore, there is no evidence on the formation of Cu-OH species, expected to generate a band at 3650 cm⁻¹, that should appear with a higher intensity at intermediate activation temperatures.⁶ This is not surprising according to the low Si/Al ratio of the parent HMOR(7), allowing Cu(II) to be stabilized by neighbouring Al sites without requiring the formation of isolated [Cu-OH]⁺ species, further confirming the 2Al 'saturation' previously hypothesized on the basis of WT-EXAFS.

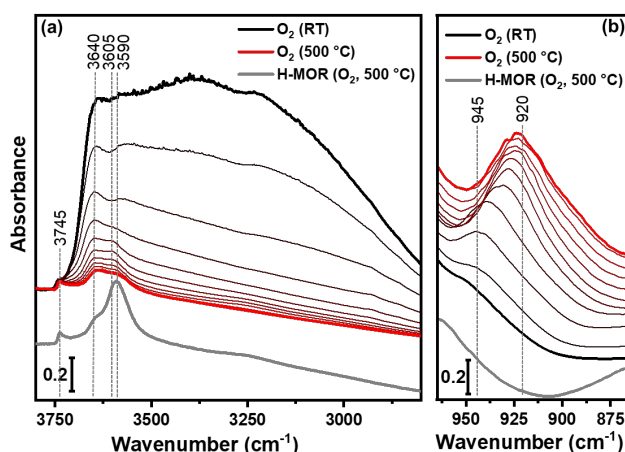


Figure 4. IR spectra of 0.18Cu-HMOR(7) during O₂ activation ramp, in the ν(OH) region (a) and in the transparency window between the ν_{asym}(T-O-T) and ν_{sym}(T-O-T) framework modes region (b). Temperature evolution from black (RT) to red (500 °C). Intermediate thin lines are equally spaced by 50 °C intervals. For the sake of comparison, the IR spectra of the HMOR(7) parent sample (activated for 2 h in O₂ flow at 500 °C) is reported in grey. The frequencies of the IR bands discussed in the text are reported (in cm⁻¹), for better clarity.

In the low frequency region (Figure 4b) we observe the evolution of the spectra of 0.18Cu-HMOR(7) upon dehydration, with the progressive growth of a band barely visible on the hydrated sample (shoulder at 945 cm⁻¹), that rises in intensity and shifts at lower frequency reaching a maximum at 920 cm⁻¹. Similar bands were observed on different zeolite-based catalysts and ascribed to the perturbation of zeolite lattice, caused by the presence of local defects.^{58, 69, 70} More specifically, the ν_{asym}(T-O-T) mode, associated with the fully absorbing feature in the 1000-1300 cm⁻¹ range, shows components at lower frequencies when the framework is perturbed by the presence of cations in close vicinity. Along the thermal treatment in oxygen, the band grows in intensity and downward shifts. This behaviour is justified by the fact that, along activation, water is progressively removed and the cations are involved in a stronger interaction with the zeolitic framework, intensifying the perturbation of the ν_{asym}(T-O-T) lattice vibrations. The observed band broadness (which is also affected by the high temperature of the measurement) testifies about the heterogeneity of the copper species local environment.

3.2.2 Key DMTM reaction steps monitored by EXAFS WT and IR

Figure 5a,b shows the *in situ* XANES and EXAFS spectra acquired for each step involved in the DMTM conversion (see inset of Figure 5a for a scheme of the followed protocol, in term of temperature profile and gas feeds). Conventional XAS analysis of these data, also presented in a previous work,²⁶ is herein integrated with the novel insights derived from EXAFS WT analysis.

O₂-activation at 500 °C results into a largely dominant Cu(II) oxidation state. The observed XAS features are consistent with tridentate O-ligated Cu(II) units, located at defined ion-exchange sites in the zeolite framework. Certain modifications are observed in the XANES spectra at the end of the O₂-activation step at 200 °C, principally regarding the white line (WL) region. In particular, a higher WL intensity is observed, pointing to a higher first-shell coordination number. A similar trend is observable analysing the related FT-EXAFS where the diminution of the temperature correlates with an increase of the intensity of the first and second shell peaks. This behaviour is primarily due to the diminution of the Debye-Waller (DW) factors as a function of the temperature. However, the thermal effect is accompanied by a structural rearranging in the first coordination sphere of Cu, upon cooling from 500 to 200 °C in O₂, as also observed in Cu-CHA.^{6, 25} A comparison of the WT-EXAFS plots for the states at 500 and 200 °C (Figure 5c - top panels) does not evidence important differences in the high-*R* range, except for a general increase of signal intensity at 200 °C, attributable to the natural reduction of DW factors at the lower data collection temperature. Importantly, we recognize a very similar morphology of WT as the one discussed in Section 3.1 for O₂-treated 0.18Cu-HMOR(7) measured *ex situ*, with sub-lobes stemming from both Cu-O/Si/Al and Cu-Cu scattering contributions.

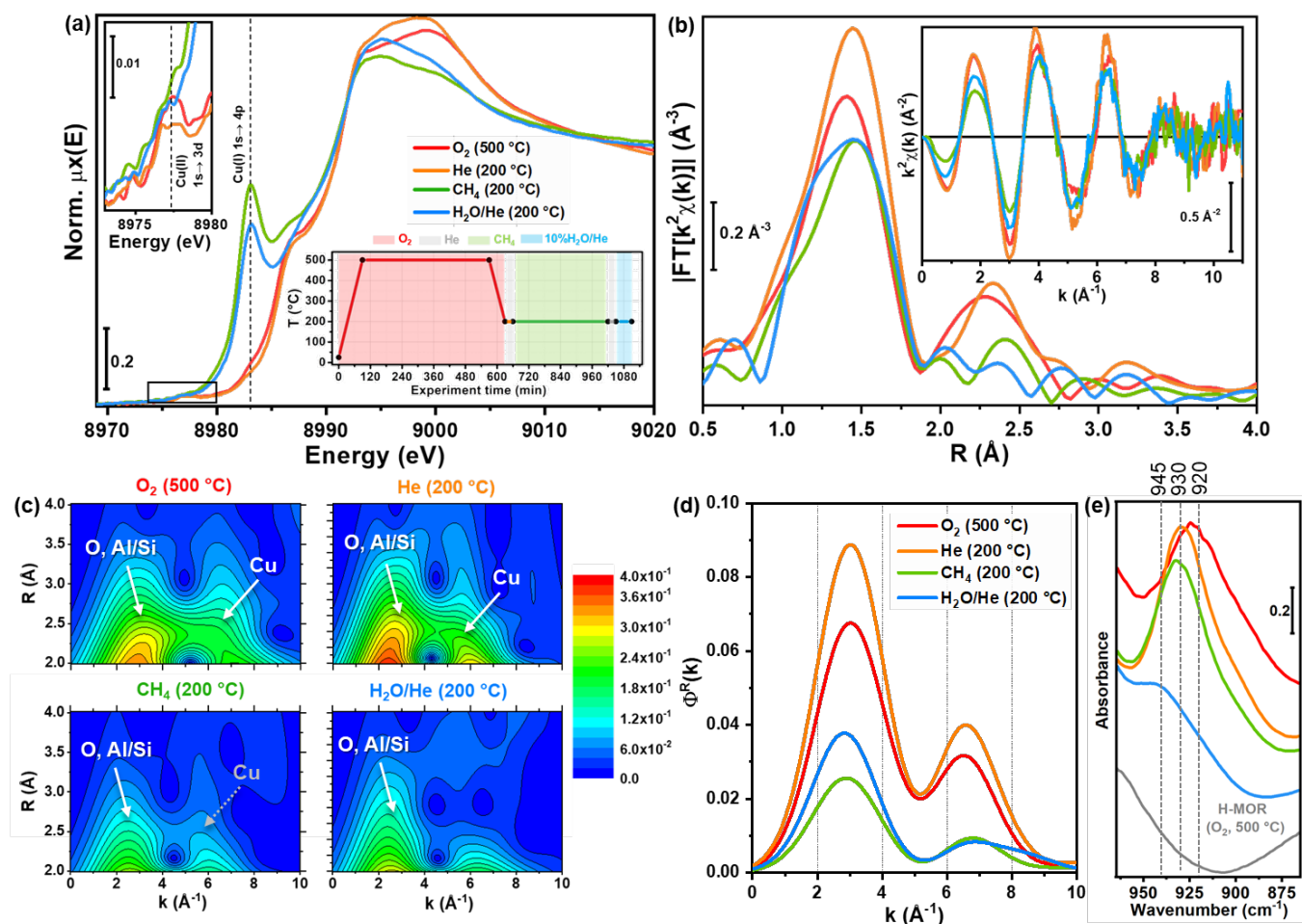


Figure 5. (a) XANES spectra of 0.18Cu-HMOR(7) after the key steps of the DMTM process. The upper inset reports a magnification of the pre-edge region. (b) $k^2\chi(k)$ signals and related magnitudes of the EXAFS-FT modulus. (c) High- R WT region for the EXAFS spectra reported in (b). WT sub-lobes stemming from O, Al/Si and Cu atomic neighbours are indicated by arrows and labels. (d) Power density functions calculated for the WT plots reported in (c). (e) IR spectra of 0.18Cu-HMOR(7) in the transparency window between the $\nu_{\text{asym}}(\text{T-O-T})$ and $\nu_{\text{sym}}(\text{T-O-T})$ framework modes region (the spectrum of parent HMOR(7) after oxidation is reported for comparison). The frequencies of the IR bands discussed in the text are reported (in cm^{-1}), for better clarity.

In agreement with previous reports exploring the potential of EXAFS-WT applied to Cu-zeolites,^{36, 41, 42} framework-coordinated Cu_xO_y species are thus confirmed to form during high-temperature O₂-activation. Such multimeric species persist with a virtually equivalent second-shell coordination environment during the subsequent cooling step in O₂, preceding to CH₄ loading.

The pronounced modifications occurring in the XAS spectra during the CH₄-loading and steam-assisted CH₃OH extraction step reflect the Cu(II) to Cu(I) reduction process and the subsequent hydration phenomena. From the spectra reported in Figure 5a,b, it is clear that Cu(I) species are formed during CH₄-loading at 200 °C and persist after the CH₃OH extraction step. This is evidenced in the XANES by the 1s → 4p rising edge peak at 8982.5 eV, characteristic of Cu(I) sites in a linear or quasi-linear coordination geometry, as already observed in the *ex situ* XAS of 0.18Cu-HMOR(7) after vacuum activation (Section 3.1). In parallel,

the first-shell intensity in the EXAFS diminishes, consistently with the formation of a fraction of two-fold coordinated Cu(I) species. At higher R -values, standard FT-EXAFS highlight a substantial decrease of the well-defined feature observed in the O₂-activated material, evolving towards an almost unstructured signal after steam-assisted CH₃OH extraction.

Wavelet analysis performed on these two steps (Figure 5c – bottom panels), evidences a simultaneous attenuation of both sub-lobes associated to framework and Cu contributions. This result is further supported from the WT power density functions $\Phi^R(k)$, calculated by eq. (8) for the four steps of the DMTM process and reported in Figure 5d. Here, we see that the contribution associated to the Cu-Cu paths, peaking at 7 Å⁻¹, undergoes a substantial attenuation after the CH₄ loading step, albeit remaining detectable. A closer look at the corresponding WT map in Figure 5c evidences a weak, residual sub-lobe in the k -range diagnostic for Cu-Cu contributions, shifting to higher R -values with respect to the O₂-activated state. After CH₃OH extraction, the Cu-Cu peak in $\Phi^R(k)$ remains very weak and further broadens so that it is difficult to resolve it as a distinct feature. Here, the features associated with low- Z scatterers in both $\Phi^R(k)$ and WT map appear slightly intensified with respect to the CH₄-loading step. Conventional FT-EXAFS shows an intensity enhancement of the low- R side of the first-shell peak, consistent with an increased coordination number in a fraction of Cu-sites, most likely undergoing to partial hydration upon exposure to steam. This translates in an average enhancement of MS contribution involving first-shell O ligands, hence accounting for the intensity increase of the WT features in the low- k range.

The structural insights emerging from WT analysis prove how the CH₄ activation at Cu-active sites is accompanied by severe rearrangements in the local coordination environment of Cu ions, involving the breakage of Cu_xO_y multimetric copper moieties, and the average elongation of interatomic distances between Cu and framework atoms. These resemble, in an inverse order, the structural transformations detected in *ex situ* experiments upon thermal treatment in O₂ of self-reduced Cu-MOR, presented in Section 3.1.

In agreement with the WT-EXAFS outcomes, also IR data collected during DMTM (Figure 5e) indicate that the local environment of Cu ions varies significantly depending on the reaction stage, as inferred by the different extent of the perturbation of the $\nu_{\text{asym}}(\text{T-O-T})$ lattice vibrations. As previously shown in Figure 4b, at the end of the O₂-activation step, a single, broad band is observed at 920 cm⁻¹, which upshifts to 930 cm⁻¹, sharpens and almost doubles in intensity as the temperature is reduced to 200 °C and the gas flow switched to He. The narrower and more symmetric shape of this peak suggests the local environment surrounding the Cu ions is more homogeneous at lower temperature. Furthermore, reduced thermal effects could also explain this spectral modification, in line with the WT-EXAFS evidences. As the oxidized sample is contacted with CH₄ for 2 h, the intensity of this band decreases, testifying the progressive modification in the coordination sphere of Cu ions. The observed effect reflects a decrease in the number

of Cu ions closely interacting with the zeolite framework, i.e. more Cu cations become unable to induce a perturbation of the $\nu_{\text{asym}}(\text{T-O-T})$ modes. Finally, upon exposure to steam in the CH_3OH extraction step, the extent of the perturbation becomes almost nil, since the band intensity drops and only a weak residual shoulder is observed at 945 cm^{-1} , comparable to that characterizing the hydrated sample prior activation (black curve in Figure 4b). The insights from *in situ* IR spectroscopy confirm the observations from WT-EXAFS, by highlighting the mobility of the Cu ions with respect to the zeolite framework as a function of the chemical environment in the different steps of the DMTM process.

3.2.3 EXAFS fitting using the WT representation

An important pre-requisite to advance in the understanding of the DMTM process is the experimental determination of the local structure of the active Cu species. Due to its sensitivity to the chemical nature of the scatterers and to the possibility to conjugate the information coming from both k -space and R -space, we propose to perform a fit of the EXAFS spectrum using the WT representation. A technical description of the strategy employed to implement this novel fitting technique is provided in Section 2.2.1.

To assess the feasibility and potential of WT EXAFS fitting, we focused on the EXAFS spectrum of O_2 -activated $0.18\text{Cu-HMOR}(7)$ after cooling to $200\text{ }^\circ\text{C}$ in O_2 and He flush (orange curves in Figure 5b). This choice is principally due to the fact that this state immediately precedes the CH_4 loading step, while ensuring a better S/N ratio with respect to the EXAFS data collected at $500\text{ }^\circ\text{C}$. Moreover, based on previous work,¹⁶ at the process conditions adopted in the *in situ* XAS experiments, this state should contain almost exclusively active dicopper Cu_2O_x moieties.

We considered a simple SS shell model for the fitting procedure. In particular, we employed a first-shell composed by both O_{fw} and O_{efw} atoms, while the signal at high- R is modelled including three separate coordination shells, involving framework Al and Si scatterers, as well as Cu atoms from multimeric copper species. The distances used to initialize the minimization procedure were defined according to available literature studies.^{6, 13, 24, 36} In the fitting procedure, for each shell, we refined the average distances $\langle R_i \rangle$ and the coordination numbers N_i , resulting into a number of guessed parameters $N^{\circ}_{\text{par}} = 9$. On the basis of previous results obtained from standard EXAFS fits of O_2 -activated Cu-zeolites,⁶ we fixed for all the SS paths a common amplitude reduction factor (S_0^2) as well as the DW factors associated to each shell; a global energy shift parameter (ΔE) was instead optimized in the fit. The fitting procedure was performed in the two dimensional range within $\Delta k=(2.4-10.5)\text{ \AA}^{-1}$ and $\Delta R=(1.0-3.5)\text{ \AA}$, resulting into a number of independent point $N^{\circ}_{\text{ind}} = 12$. Figure 6 compares experimental and best-fit full-range WT plots while the results of the WT fitting procedure are reported in Table 1.

The best-fit WT plot in Figure 6a properly reproduces all the main features associated to the experimental WT features, as quantified by the R-factor associated to the reconstruction, equal to 0.01. At the same

time, from the graphical analysis of the individual WT contributions in Figure 6b, it is possible to observe how their location in the (k, R) space falls in line with the qualitative analysis and the assignments provided before.

Fitting results support the dominant presence of di-copper species ($N_{\text{Cu}} \sim 1$) surrounded by a first shell of O atoms with coordination number $N_{\text{O}} \sim 3$. The number of Al and Si atoms, identified by the fit, is refined to ca. 1 and 2 respectively. These values are in accordance with the coordination numbers associated to Al and Si shells previously found in O_2 activated Cu-zeolites.^{6, 13} At the same time, the optimized interatomic distances are consistent with the DFT values retrieved by precedent theoretical works.^{36, 61, 62} Based on these available models for Cu local environment, we can envisage the presence of two O_{fw} and one O_{efw} atoms, bridging the two Cu centres. A possible configuration compatible with the obtained results could involve Cu-mono-(μ -oxo) dimers. The presence of Cu-peroxo dicopper species with an end-on O_2 -binding mode is instead discouraged, based on the Cu-Cu distance found by the fit. Indeed, the optimized value of $\langle R_{\text{Cu}} \rangle \sim 3.1 \text{ \AA}$ is significantly shorter than the DFT value of ca. 4.3 \AA predicted for the latter species in Cu-MOR.³⁶

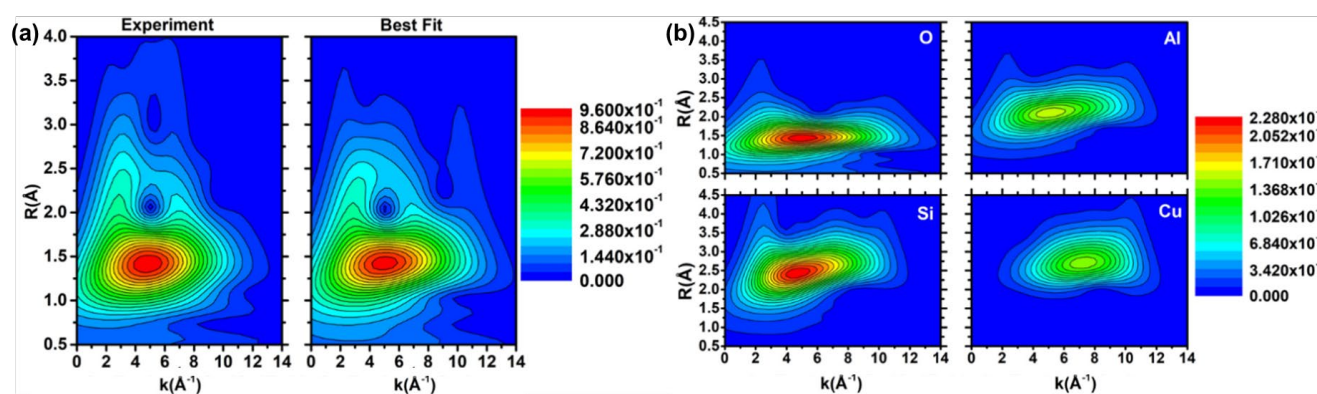


Figure 6. (a) Comparison between the best fit and the experimental WT representation of the EXAFS signal acquired on O_2 -activated 0-18Cu-HMOR(7). (b) WT representation associated to the individual scattering contributions (Cu-O, Cu-Al, Cu-Si and Cu-Cu) extracted from the fit. The intensity for the Cu-O contribution (top left plot) refers to the colour scale displayed in part (a), whereas all the other (high- R) contributions have been plotted according to the colour scale reported in part (b), to facilitate comparison among the relevant WT features.

Table 1. Results of the WT EXAFS fit for O₂-activated 0.18Cu-HMOR(7) after cooling to 200 °C in O₂ and He flush (orange curves in Figure 5b). The parameters fixed in the fit are underlined.

Best Fit Parameters	
ΔR (Å)	2.5
Δk (Å ⁻¹)	8.1
N ^o _{par} /N ^o _{ind}	9/12
R _{factor}	0.01
<u>S₀²</u>	<u>0.9</u>
ΔE (eV)	-1.93 ± 0.07
$\langle R_O \rangle$ (Å)	1.939 ± 0.001
$\langle R_{Al} \rangle$ (Å)	2.724 ± 0.002
$\langle R_{Cu} \rangle$ (Å)	3.112 ± 0.003
$\langle R_{Si} \rangle$ (Å)	3.138 ± 0.003
<u>σ_O^2 (Å²)</u>	<u>0.004</u>
<u>σ_{Al}^2 (Å²)</u>	<u>0.006</u>
<u>σ_{Cu}^2 (Å²)</u>	<u>0.007</u>
<u>σ_{Si}^2 (Å²)</u>	<u>0.008</u>
N _O	3.03 ± 0.01
N _{Al}	0.90 ± 0.02
N _{Cu}	0.99 ± 0.03
N _{Si}	2.22 ± 0.04

It is worth to note that several constraints have been adopted in this initial, exploratory EXAFS-WT fit. We preferred to consider a single O shell entailing both O_{fw} and O_{efw}, to fix DW factors and neglect the farther O atoms of the zeolite lattice. With these choices, we aimed at building a flexible structural model, capable of describing different types of Cu-species to obtain a first screening on the most likely configuration. Having now assessed the validity of the method, future works will involve EXAFS WT-fits using an appropriate set of DFT-optimized structures to initialize the fitting model, where different Cu dimeric configurations will be explored more systematically.

Finally, a note on the estimation of the fit errors is deserved. Indeed, it is possible to observe that the optimized parameters, especially the coordination numbers, are associated to quite low error values. This could be caused by: (i) the impossibility to define a proper set of experimental errors which could be used in the χ^2 definition, see eq. (7); (ii) the failure in the estimation of the standard errors from the covariance matrix. In the future, we envisage to address these two possible sources of error underestimation by: (i) extending the Parseval formula⁷¹ to the WT domain, thus deriving the errors associated to each point of the 2D grid of the WT through the error estimated in the k/R space; (ii) exploiting the F-test to identify properly the confidence intervals associated to each free parameter, according with ref.⁷²

4. Conclusions

In this work, we have applied wavelet transform (WT) as an alternative approach in EXAFS data visualization and analysis, aiming at enhancing the sensitivity of the technique towards multimeric Cu-species in zeolites. As a case study to assess the potential of this methodology, we have selected Cu-MOR zeolites for the

DMTM conversion, characterized by XAS both *ex situ*, under model conditions resulting into Cu(I) and Cu(II) states, and *in situ*, along the key DMTM reaction steps over the most productive material, 0.18Cu-HMOR(7). Overall, the reported results demonstrate how Cu-Cu scattering contributions can be successfully distinguished from those involving lower-Z atoms (O, Al/Si) through a diagnostic sub-lobe in WT-EXAFS maps, centred at ca. 7 \AA^{-1} in *k*-space.

WT-EXAFS analysis of Cu-MOR samples with different compositional characteristics provides direct evidences for the presence of Cu(I)···Cu(I) pairs in the vacuum activated, self-reduced state. Thermal treatment in O₂ causes substantial rearrangements in the local coordination environment of Cu ions, similarly to what predicted by Tsai et al.⁶⁴ Upon oxidation, Cu atoms are observed to approach the zeolite framework and to re-organize with shorter Cu-Cu separations, consistently with the formation of multimeric Cu-oxo cores. Aided by WT power density functions $\Phi^R(\mathbf{k})$, we rationalize the intensity trends observed for Cu-Cu features as a function of the compositional parameters through a possible saturation mechanism of 2Al sites, driving the docking of Cu ions to zeolite lattice along dehydration.

Such dynamical response of Cu coordination motifs to the chemical environment is then also recognized during the key steps of DMTM, according to the complementary views provided by EXAFS-WT analysis and IR spectroscopy. Framework-coordinated multimeric Cu-oxo species are unambiguously detected in the O₂-activated state, with a WT plane morphology resembling the one detected in the *ex situ* study upon thermal treatment in O₂. Upon CH₄ loading and subsequent steam-assisted CH₃OH extraction, EXAFS-WT highlights the breakage of Cu_xO_y multimeric moieties together with the increase of interatomic distances between Cu ions and zeolite framework. The latter finding is also corroborated by IR results, showing a weaker perturbation of the $\nu_{\text{asym}}(\text{T-O-T})$ lattice vibration.

We finally move from qualitative to quantitative utilisation of WT-EXAFS, proposing an EXAFS fitting procedure based on the wavelet representation. WT EXAFS fit of the O₂-activated state measured *in situ* for 0.18Cu-HMOR(7) revealed a local structure compatible with mono-(μ -oxo) di-copper cores, with Cu-Cu separation of $\sim 3.1 \text{ \AA}$. Albeit obtained using a simplified model, the fitting results are encouraging and will pave the way to improved implementations of the method.

Taken together, the results reported here for Cu-MOR highlight the potential of WT EXAFS analysis, used as a visual diagnostic tool or even for quantitative structural refinement, in challenging situations where multiple scattering contributions/interactions overlap in the same *R*-space range.

Conflicts of interest

There are no conflicts to declare.

Acknowledgements

This publication forms a part of the iCSI (industrial Catalysis Science and Innovation) Centre for Research-based Innovation, which receives financial support from the Research Council of Norway under Contract No. 237922. The authors are grateful to D.K. Pappas, M. Dyballa, Unni Olsbye, K.P. Lillerud (University of Oslo) and B. Arstad (SINTEF) for their contribution to the study of DMTM over Cu-zeolites, fruitful advices and support. We also thank A.A. Guda and S.A. Guda (Southern Federal University) for insightful discussion about the WT-EXAFS fitting procedure.

Notes and references

1. P. Tang, Q. Zhu, Z. Wu and D. Ma, *Energ. Environ. Sci.*, 2014, **7**, 2580-2591.
2. G. A. Olah, G. K. S. Prakash and A. Goepfert, *J. Am. Chem. Soc.*, 2011, **133**, 12881-12898.
3. M. Ravi, V. L. Sushkevich, A. J. Knorpp, M. A. Newton, D. Palagin, A. B. Pinar, M. Ranocchiari and J. A. van Bokhoven, *Nature Catal.*, 2019, **2**, 485-494.
4. D. Park and J. Lee, *Korean J. Chem. Eng.*, 2013, **30**, 977-987.
5. M. H. Groothaert, P. J. Smeets, B. F. Sels, P. A. Jacobs and R. A. Schoonheydt, *J. Am. Chem. Soc.*, 2005, **127**, 1394-1395.
6. D. K. Pappas, E. Borfecchia, M. Dyballa, I. A. Pankin, K. A. Lomachenko, A. Martini, M. Signorile, S. Teketel, B. Arstad, G. Berlier, C. Lamberti, S. Bordiga, U. Olsbye, K. P. Lillerud, S. Svelle and P. Beato, *J. Am. Chem. Soc.*, 2017, **139**, 14961-14975.
7. S. Grundner, M. A. C. Markovits, G. Li, M. Tromp, E. A. Pidko, E. J. M. Hensen, A. Jentys, M. Sanchez-Sanchez and J. A. Lercher, *Nat. Commun.*, 2015, **6**, 9.
8. E. M. C. Alayon, M. Nachtegaal, A. Bodi and J. A. van Bokhoven, *ACS Catal.*, 2014, **4**, 16-22.
9. V. L. Sushkevich, D. Palagin, M. Ranocchiari and J. A. van Bokhoven, *Science*, 2017, **356**, 523-527.
10. P. Tomkins, A. Mansouri, S. E. Bozbag, F. Krumeich, M. B. Park, E. M. C. Alayon, M. Ranocchiari and J. A. van Bokhoven, *Angew. Chem. Int. Ed.*, 2016, **55**, 5467-5471.
11. A. J. Knorpp, M. A. Newton, S. C. M. Mizuno, J. Zhu, H. Mebrate, A. B. Pinar and J. A. van Bokhoven, *Chem. Commun.*, 2019, **55**, 11794-11797.
12. P. Vanelderen, J. Vancauwenbergh, M.-L. Tsai, R. G. Hadt, E. I. Solomon, R. A. Schoonheydt and B. F. Sels, *ChemPhysChem*, 2014, **15**, 91-99.
13. E. M. C. Alayon, M. Nachtegaal, A. Bodi, M. Ranocchiari and J. A. van Bokhoven, *Phys. Chem. Chem. Phys.*, 2015, **17**, 7681-7693.
14. S. E. Bozbag, E. M. C. Alayon, J. Pecháček, M. Nachtegaal, M. Ranocchiari and J. A. van Bokhoven, *Catal. Sci. Technol.*, 2016, **6**, 5011-5022.
15. B. E. R. Snyder, P. Vanelderen, R. A. Schoonheydt, B. F. Sels and E. I. Solomon, *J. Am. Chem. Soc.*, 2018, **140**, 9236-9243.
16. D. K. Pappas, A. Martini, M. Dyballa, K. Kvande, S. Teketel, K. A. Lomachenko, R. Baran, P. Glatzel, B. Arstad, G. Berlier, C. Lamberti, S. Bordiga, U. Olsbye, S. Svelle, P. Beato and E. Borfecchia, *J. Am. Chem. Soc.*, 2018, **140**, 15270-15278.
17. D. Palagin, A. J. Knorpp, A. B. Pinar, M. Ranocchiari and J. A. van Bokhoven, *Nanoscale*, 2017, **9**, 1144-1153.
18. V. L. Sushkevich, D. Palagin and J. A. van Bokhoven, *Angew. Chem. Int. Edit.*, 2018, **57**, 8906-8910.
19. A. M. Beale, F. Gao, I. Lezcano-Gonzalez, C. H. F. Peden and J. Szanyi, *Chem. Soc. Rev.*, 2015, **44**, 7371-7405.
20. C. Paolucci, I. Khurana, A. A. Parekh, S. Li, A. J. Shih, H. Li, J. R. Di Iorio, J. D. Albarracin-Caballero, A. Yezerets, J. T. Miller, W. N. Delgass, F. H. Ribeiro, W. F. Schneider and R. Gounder, *Science*, 2017, **357**, 898-903.
21. E. Borfecchia, P. Beato, S. Svelle, U. Olsbye, C. Lamberti and S. Bordiga, *Chem. Soc. Rev.*, 2018, **47**, 8097-8133.
22. F. Gao and C. H. F. Peden, *Catalysts*, 2018, **8**, 140.

23. E. Borfecchia, K. A. Lomachenko, F. Giordanino, H. Falsig, P. Beato, A. V. Soldatov, S. Bordiga and C. Lamberti, *Chem. Sci.*, 2015, **6**, 548-563.
24. C. Buono, A. Martini, I. A. Pankin, D. K. Pappas, C. Negri, K. Kvande, K. A. Lomachenko and E. Borfecchia, *Radiat. Phys. Chem.*, in press, doi: 10.1016/j.radphyschem.2018.1012.1031.
25. E. Borfecchia, D. K. Pappas, M. Dyballa, K. A. Lomachenko, C. Negri, M. Signorile and G. Berlier, *Catal. Today*, 2019, **333**, 17-27.
26. K. A. Lomachenko, A. Martini, D. K. Pappas, C. Negri, M. Dyballa, G. Berlier, S. Bordiga, C. Lamberti, U. Olsbye, S. Svelle, P. Beato and E. Borfecchia, *Catal. Today*, 2019, **336**, 99-108.
27. M. A. Newton, A. J. Knorpp, A. B. Pinar, V. L. Sushkevich, D. Palagin and J. A. van Bokhoven, *J. Am. Chem. Soc.*, 2018, **140**, 10090-10093.
28. K. Kvande, D. K. Pappas, E. Borfecchia and K. A. Lomachenko, *ChemCatChem*, 2020, **12**, 2385-2405.
29. S. Bordiga, E. Groppo, G. Agostini, J. A. van Bokhoven and C. Lamberti, *Chem. Rev.*, 2013, **113**, 1736-1850.
30. K. A. Lomachenko, E. Borfecchia, S. Bordiga, A. V. Soldatov, P. Beato and C. Lamberti, *J. Phys.: Conf. Ser.*, 2016, **712**, 012041.
31. E. I. Solomon, D. E. Heppner, E. M. Johnston, J. W. Ginsbach, J. Cirera, M. Qayyum, M. T. Kieber-Emmons, C. H. Kjaergaard, R. G. Hadt and L. Tian, *Chem. Rev.*, 2014, **114**, 3659-3853.
32. B. E. R. Snyder, M. L. Bols, R. A. Schoonheydt, B. F. Sels and E. I. Solomon, *Che. Rev.*, 2018, **118**, 2718-2768.
33. A. Voronov, A. Urakawa, W. v. Beek, N. E. Tsakoumis, H. Emerich and M. Rønning, *Anal. Chim. Acta*, 2014, **840**, 20-27.
34. A. Martini, E. Borfecchia, K. A. Lomachenko, I. A. Pankin, C. Negri, G. Berlier, P. Beato, H. Falsig, S. Bordiga and C. Lamberti, *Chem. Sci.*, 2017, **8**, 6836-6851.
35. P. Glatzel and U. Bergmann, *Coord. Chem. Rev.*, 2005, **249**, 65-95.
36. I. A. Pankin, A. Martini, K. A. Lomachenko, A. V. Soldatov, S. Bordiga and E. Borfecchia, *Catal. Today*, 2020, **345**, 125-135.
37. C. Paolucci, A. A. Parekh, I. Khurana, J. R. Di Iorio, H. Li, J. D. A. Caballero, A. J. Shih, T. Anggara, W. N. Delgass, J. T. Miller, F. H. Ribeiro, R. Gounder and W. F. Schneider, *J. Am. Chem. Soc.*, 2016, **138**, 6028-6048.
38. H. Funke, A. C. Scheinost and M. Chukalina, *Phys. Rev. B*, 2005, **71**, 7.
39. M. Munoz, P. Argoul and F. Farges, *Am. Miner.*, 2003, **88**, 694-700.
40. J. Timoshenko and A. Kuzmin, *Comput. Phys. Commun.*, 2009, **180**, 920-925.
41. A. Martini, I. A. Pankin, A. Marsicano, K. A. Lomachenko and E. Borfecchia, *Radiat. Phys. Chem.*, in press, doi: 10.1016/j.radphyschem.2019.1005.1023.
42. V. L. Sushkevich, O. V. Safonova, D. Palagin, M. A. Newton and J. A. van Bokhoven, *Chem. Sci.*, 2020, **11**, 5299-5312.
43. O. Mathon, A. Beteva, J. Borrel, D. Bugnazet, S. Gatla, R. Hino, I. Kantor, T. Mairs, M. Munoz, S. Pasternak, F. Perrin and S. Pascarelli, *J. Synchrotron Radiat.*, 2015, **22**, 1548-1554.
44. G. Agostini, D. Meira, M. Monte, H. Vitoux, A. Iglesias-Juez, M. Fernandez-Garcia, O. Mathon, F. Meunier, G. Berruyer, F. Perrin, S. Pasternak, T. Mairs, S. Pascarelli and B. Gorges, *J. Synchrotron Radiat.*, 2018, **25**, 1745-1752.
45. B. Ravel and M. Newville, *J. Synchrotron Radiat.*, 2005, **12**, 537-541.
46. M. A. Soldatov, A. Martini, A. L. Bugaev, I. Pankin, P. V. Medvedev, A. A. Guda, A. M. Aboraia, Y. S. Podkovyrina, A. P. Budnyk, A. A. Soldatov and C. Lamberti, *Polyhedron*, 2018, **155**, 232-253.
47. T. J. Penfold, I. Tavernelli, C. J. Milne, M. Reinhard, A. El Nahhas, R. Abela, U. Rothlisberger and M. Chergui, *J. Chem. Phys.*, 2013, **138**, 7.
48. M. Newville, *J. Synchrotron Radiat.*, 2001, **8**, 322-324.
49. J. J. Rehr, J. J. Kas, M. P. Prange, A. P. Sorini, Y. Takimoto and F. Vila, *C. R. Phys.*, 2009, **10**, 548-559.
50. S. I. Zabinsky, J. J. Rehr, A. Ankudinov, R. C. Albers and M. J. Eller, *Phys. Rev. B*, 1995, **52**, 2995-3009.
51. M. Newville, *J. Synchrotron Radiat.*, 2001, **8**, 96-100.
52. A. Kuzmin, *Physica B*, 1995, **208**, 175-176.

53. J. J. Moré, *The Levenberg-Marquardt algorithm: Implementation and theory*, Berlin, Heidelberg, 1978.
54. G. Bunker, *Introduction to XAFS: A Practical Guide to X-ray Absorption Fine Structure Spectroscopy*, Cambridge University Press, New York, 2010.
55. S. Calvin, *XAFS for Everyone*, Taylor & Francis, Boca Raton, 2013.
56. M. Newville, T. Stensitzki, D. B. Allen and A. Ingargiola, *Zenodo*, 2014, doi: <http://doi.org/10.5281/zenodo.11813>.
57. P. Virtanen, R. Gommers, T. E. Oliphant, M. Haberland, T. Reddy, D. Cournapeau, E. Burovski, P. Peterson, W. Weckesser, J. Bright, et al., *Nat. Methods*, 2020, **17**, 261–272.
58. G. Turnes Palomino, P. Fiscaro, S. Bordiga, A. Zecchina, E. Giamello and C. Lamberti, *J. Phys. Chem. B*, 2000, **104**, 4064-4073.
59. V. L. Sushkevich and J. A. van Bokhoven, *Chem. Commun.*, 2018, **54**, 7447-7450.
60. T. V. W. Janssens, H. Falsig, L. F. Lundegaard, P. N. R. Vennestrom, S. B. Rasmussen, P. G. Moses, F. Giordanino, E. Borfecchia, K. A. Lomachenko, C. Lamberti, S. Bordiga, A. Godiksen, S. Mossin and P. Beato, *ACS Catal.*, 2015, **5**, 2832-2845.
61. P. Vanelderen, B. E. Snyder, M. L. Tsai, R. G. Hadt, J. Vancauwenbergh, O. Coussens, R. A. Schoonheydt, B. F. Sels and E. I. Solomon, *J. Am. Chem. Soc.*, 2015, **137**, 6383-6392.
62. L. Vilella and F. Studt, *Eur. J. Inorg. Chem.*, 2016, **2016**, 1514-1520.
63. H. Funke, M. Chukalina and A. C. Scheinost, *J. Synchrotron Radiat.*, 2007, **14**, 426-432.
64. M. L. Tsai, R. G. Hadt, P. Vanelderen, B. F. Sels, R. A. Schoonheydt and E. I. Solomon, *J. Am. Chem. Soc.*, 2014, **136**, 3522-3529.
65. J. Dedecek, V. Balgova, V. Pashkova, P. Klein and B. Wichterlova, *Chem. Mat.*, 2012, **24**, 3231-3239.
66. J. R. Di Iorio and R. Gounder, *Chem. Mat.*, 2016, **28**, 2236-2247.
67. I. R. Subbotina, B. N. Shelimov and V. B. Kazanskii, *Kinet. Catal.*, 2002, **43**, 412-418.
68. V. L. Zholobenko, M. A. Makarova and J. Dwyer, *J. Phys. Chem.*, 1993, **97**, 5962-5964.
69. D. Scarano, A. Zecchina, S. Bordiga, F. Geobaldo, G. Spoto, G. Petrini, G. Leofanti, M. Padovan and G. Tozzola, *J. Chem. Soc., Faraday Trans.*, 1993, **89**, 4123-4130.
70. G. Ricchiardi, A. Damin, S. Bordiga, C. Lamberti, G. Spanò, F. Rivetti and A. Zecchina, *J. Am. Chem. Soc.*, 2001, **123**, 11409-11419.
71. M. Newville, B. I. Boyanov and D. E. Sayers, *J. Synchrotron Radiat.*, 1999, **6**, 264-265.
72. A. Filippini and A. DiCiccio, *Phys. Rev. B*, 1995, **52**, 15135-15149.